Mechanical behavior of representative volume elements of lithium-ion battery cells under compressive loading conditions

Wei-Jen Lai [a], Mohammed Yusuf Ali [b], Jwo Pan [b],*

[a] Department of Materials Science and Engineering, The University of Michigan, Ann Arbor, MI 48109, USA
[b] Department of Mechanical Engineering, The University of Michigan, Ann Arbor, MI 48109, USA

HIGHLIGHTS

- Present stress–strain curves for LiFePO$_4$ battery cells under in-plane constrained compression.
- Correlate experimental stress–strain curves to deformation patterns of battery cells.
- Model the buckling of cell specimens and justify the length selection of cell specimens.
- Correlate the buckling of cell components to the buckling stress of battery cells.
- Present a physical kinematic model for formation of kinks and shear bands in battery cells.

ARTICLE INFO

ABSTRACT

The mechanical behaviors of lithium iron phosphate battery cells are investigated by conducting in-plane and out-of-plane compression tests of representative volume element (RVE) specimens of dry cells. The test results of cell RVE specimens under in-plane constrained compression indicate that the load carrying behavior of the cell RVE specimens is characterized by the buckling, the kink and shear band formation, and the final densification of the cell components. The SEM images of the active materials on electrodes and the test results of the cell RVE specimens under out-of-plane compression suggest that the porosity in the components and the macroscopic gaps between the components is up to 40%. The test results suggest that the lithium-ion battery cells can be modeled as anisotropic foams or cellular materials. The elastic buckling analyses for a beam with lateral constraints indicate that the higher order buckling modes and the critical buckling stresses in general agree with those observed in experiments. The elastic buckling analyses also justify the length selection of the cell RVE specimens. Finally, an idealized kinematic model is presented to explain the physical mechanisms of the kink and shear band formation in the cell RVE specimens under in-plane constrained compression.

1. Introduction

Lithium-ion batteries have been considered as the solution for electric vehicles for the automotive industry due to its lightweight and high energy density. The major design considerations for lithium-ion batteries involve electrochemistry, thermal management and mechanical performance. The electrochemistry has been widely studied since it directly determines the battery performance and its life cycle. Different active materials on electrodes form different types of lithium-ion batteries. However, the basic chemical reactions of battery cells are similar. For automotive applications, the mechanical performance is of great importance for crashworthiness analyses. Mechanical tests such as shock, drop, penetration, roll-over, and crush tests for abuse conditions of battery cells, modules and packs were documented in SAE J2462 [1]. Research works were conducted on the safety performance of the battery cells under mechanical tests such as nail penetration tests, round bar crush tests, and pinch tests, for example, see Refs. [2–4]. However, the research works on the mechanical behavior of the representative volume elements (RVEs) of lithium-ion batteries are quite limited.

Sahraei et al. [5] conducted a series of mechanical tests and computational works on commercial LiCoO$_2$/graphite cells used for

* Corresponding author. Tel.: +1 734 764 9404; fax: +1 734 647 3170.
E-mail addresses: weijen@umich.edu (W.-J. Lai), mdyusuf@umich.edu (M.Y. Ali), jwo@umich.edu, jwopan@gmail.com (J. Pan).

Nomenclature

RVE	representative volume element
ROM	rule of mixture
P_m^i	buckling load of the i-th component with the two unattached elastic foundation
m	number of half waves
E_i	compressive elastic modulus of the i-th component
$I_i = bh_i^3/12$	moment of inertia of the i-th component
L	length of the cell component
p	lateral pressure on the beam
z	deflection of the beam
k_1, k_2	spring constants of the harder and softer elastic foundations on the two sides of the beam
$\phi = k_1/k_2$	spring constant ratio
α	coefficient depending upon the value of m in Equation (1)
$\overline{m}$	parameter defined in Equation (2)
b	width of the cell component
h_i	thickness of the i-th component
E_i'	effective compressive elastic modulus of the i-th component under plane strain compression conditions
E_i	compressive elastic modulus of the i-th component
ν_i	Poisson's ratio of the i-th component
k	spring constant of the elastic foundation
E	out-of-plane compressive elastic modulus of the cell RVE specimen
h	thickness of the neighbor cell components
P_c^i	critical buckling load of the i-th component
P_n^i	buckling load of the i-th component with an unattached elastic foundation on one side and a rigid wall on the other side
n	number of waves
$\overline{n}$	parameter defined in Equation (10)
ε_m^i	compressive strain of the i-th component with the two unattached elastic foundation
ε_n^i	compressive strain of the i-th component with an unattached elastic foundation on one side and a rigid wall on the other side
A_i	cross sectional area of the i-th component
P_{cell}	buckling load of cell RVE specimen
n_i	number of the i-th component in the cell RVE specimen
σ_{cell}	buckling stress of the cell RVE specimen
A	cross sectional area of the cell RVE specimen
α	kink angle
w	width of the cell RVE specimen
d	kink length
θ	shear band angle
θ_i	initial shear band angle
θ_f	final shear band angle
$\varepsilon_{Y'}$	nominal normal strain in Y' direction
$\varepsilon_{Z'}$	nominal normal strain in Z' direction
$\gamma_{Y'Z'}$	nominal shear strain in $Y'Z'$ plane
ε_Y^T	total nominal strain of one unit cell in cell RVE specimen
h_s	shear band height
E_{cell}'	effective compressive elastic modulus of the cell RVE specimen
f_i	volume fraction of the i-th component
f	void volume fraction

cell phones. The results indicate that the compressive mechanical behavior is characterized by the buckling and densification of the cell components. Other testing and modeling data available were also conducted on commercial LiCoO$_2$ cylindrical or prismatic battery cells [6,7]. However, this information is of limited use for researchers to model the mechanical performance of automotive high-voltage LiFePO$_4$ battery cells and modules for crashworthiness analyses. Sahraei et al. [5] indicated that computational effort is quite significant to model local buckling phenomenon of battery cells under in-plane compression. Therefore, macro homogenized material models of the representative volume elements (RVEs) for both the battery cells and modules have to be developed for crashworthiness analyses with sacrifice of the accuracy at the micro scale.

One of the primary objectives of this investigation is to develop testing methods to determine the detailed mechanical properties of lithium-ion battery cells and modules [8] in a systematic fashion. The other is to provide the necessary experimental data for the development of macro homogenized material models in the companion papers [9,10]. At this point, there is no test standard for characterizing the mechanical properties of the representative volume elements (RVEs) of lithium-ion batteries under large deformation because it is difficult to test a live battery due to the safety concern. Even in the discharged state, the volatile and toxic electrolyte still poses a severe safety concern. Further, standard compression tests in an in-plane direction of cell specimens do not provide useful information since there are almost no bonding forces between the anode, cathode, separator and cover sheets. The cell specimens fall apart when no out-of-plane constraints are applied. Therefore, a constrained compression test procedure needs to be developed and provide other researchers a way to conduct tests and compare the test results. The results presented in this paper can also help to understand the deformation process and mechanical behavior of battery cells such that homogenized material models can be developed for battery cells.

One ultimate goal of this investigation is to provide test data for development of computational models for multi-scale multi-physics analyses of battery packs in vehicles under crash loading conditions. Battery pack designs are different for different electric vehicles. Battery packs can have various shapes of plastic or metal shells that enclose a cooling system, electronics, and battery modules, that contain battery cells with electronics cover plates, control electronics, pressure plates, laser welded bus bars, heat sink plates, interconnected covers and compression bands. Battery pack designs are usually quite complex. Different types of finite elements such as shell elements, solid elements, rigid elements, and weld elements are typically used in computational models to reduce the sizes of the models. However, the sizes of the computational models for battery packs can still be quite large for crashworthiness analyses since the sizes of finite elements have to be small with consideration of small thicknesses of pack components and deformation patterns of interest. It is not possible to model the details of all battery pack components for computational efficiency in full vehicle crashworthiness analyses.

Finite element models for small cell specimens under compression in Sahraei et al. [5] showed the complexity of the finite element analyses at the length scale of cell components. Finite element models for cell RVE specimens under in-plane constrained compression in Ali et al. [9] also showed the complexity of the finite element analyses at the length scale of cell components. Sahraei et al.
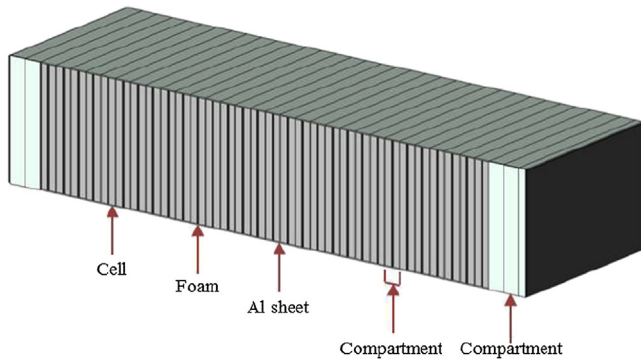
Fig. 1. A typical battery module.

[7] conducted finite element analyses of an idealized battery pack with an outer steel shell and a homogenized crushable foam core to simulate a drop test of the battery pack on a rigid cylinder. The results showed that with the homogenized foam model, it was computationally efficient to model the drop test of the battery pack for optimum design. Ali et al. [10] conducted finite element analyses of a small-scale module specimen under in-plane punch indentation [8] based on several homogenized material models. The computational results indicated that it was computationally efficient to simulate the module specimen under punch indentation with the homogenized material models. Therefore, homogenized material models for cells and modules can be quite useful for simulation and control of the crush responses of battery packs for optimum design under crash loading conditions with computational efficiency. Based on homogenized material models, computational results for deformed battery cells from full vehicle crashworthiness analyses can then be used for further combined structural, electrical and thermal analyses of battery cells at the smaller length scales.

In this investigation, cell RVE specimens were first made from the individual cell components and in-plane constrained compression tests were then conducted. Out-of-plane compression tests of cell RVE specimens were also conducted to understand the different behaviors in the in-plane and out-of-plane directions. Based on the experimental observations of the cell RVE specimens under in-plane constrained compression and the results of the corresponding finite element analyses, the buckling mode of the cell RVE specimens under in-plane constrained compression is examined by elastic buckling analyses of a beam with lateral constraints. The buckling loads for the cell RVE specimens are then obtained based on the elastic buckling solutions and the composite rule of mixture (ROM). In addition, an idealized kinematic model is developed to explain the physical mechanisms of the kink and shear band formation in the cell RVE specimens under in-plane constrained compression. Finally, some conclusions are made.

2. Specimens

The structure of a typical battery module based on prismatic pouch cells is shown in Fig. 1. The module is composed of many compartments (shown as several light blue compartments on both ends of the module in the web version) separated by aluminum heat dissipater sheets (shown in light blue). Inside each compartment (in the middle portion of the module where the side aluminum heat dissipater sheet is removed), there are two cells (shown in gray) with one layer of foam (shown in black) between the two cells. The battery module is usually held together by two stainless steel bands (not shown) with a specified tension and the adhesive (between the cell and the foam layer, and between the cell and the aluminum heat dissipater sheet).

Each cell consists of five major components: cover sheet, anode, cathode, separator and electrolyte. Since the electrolyte is difficult to handle during assembly due to its toxicity, all the cell RVE specimens tested in this study were made without electrolyte at the University of Michigan. Table 1 lists all the detailed material and thickness information of the cell components. The cover sheet is composed of aluminum foil with polyamide and polypropylene layers on both sides bonded together by polyester—polyurethane and urethane-free adhesive, respectively. The thicknesses of the individual layers of the cover sheet are shown in Table 1 and the total thickness of the cover sheet is 0.111 mm. The anode and cathode selected for this study are graphite coated on copper foil and LiFePO$_4$ coated on aluminum foil, respectively. The copper foil has a thickness of 9 μm and the total thickness of the anode sheet is 0.2 mm. The aluminum foil has a thickness of 15 μm and the total thickness of the cathode sheet is 0.2 mm. Both the anode and cathode sheets are double-side coated. The SEM images of the graphite and LiFePO$_4$ on the anode and cathode sheets are shown in Fig. 2(a) and (b), respectively. It is noted that both active materials on the electrodes are in a powder form held together by binders and therefore possess a high degree of porosity. It is not the intent of this investigation to characterize the morphology of the active materials. The separator is made of polyethylene with the porosity ranging from 36 to 44% and a thickness from 16 to 25 μm. All the cell components are purchased commercially.

Fig. 3(a) shows a schematic of a pouch cell and a cell RVE specimen with the X−Y−Z coordinate system. Here, X and Y are referred to as the in-plane directions and Z is referred to as the out-of-plane plane direction. A small cell RVE specimen with the dimensions is shown in Fig. 3(b). Fig. 3(c) shows a side view of a portion of a cell RVE specimen with the individual cell components. The large red arrows shown in the figures indicate the in-plane compressive direction. As shown in Fig. 3(c), the anodes

Table 1
Specifications of cell components.

	Material	Thickness		Notes
Cover sheet	Polyamide (JIS Z1714)	0.025 mm	0.111 mm	
	Adhesive (polyester—polyurethane)	4–5 g m^{-2}		
	Aluminum foil (JIS A8079, A8021)	0.040 mm		
	Adhesive (urethane-free adhesive)	2–3 g m^{-2}		
	Polypropylene	0.040 mm		
Anode	Copper foil	9 μm	0.2 mm	Double side coated
	Graphite			Binder: SBR + CMC
Cathode	Aluminum foil	15 μm	0.2 mm	Double side coated
	LiFePO$_4$			
Separator	Polyethylene (PE)	16–25 μm		Porosity: 36%–44%
				Pore size: 0.01–0.1 μm
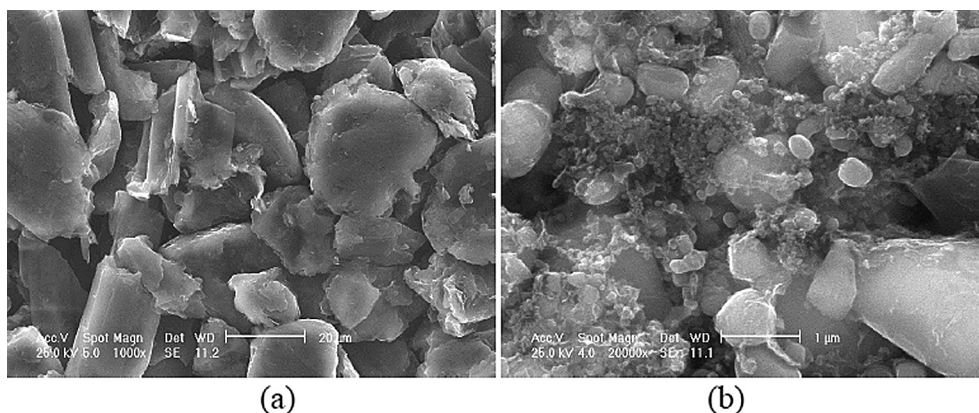
Fig. 2. SEM images of (a) graphite and (b) LiFePO$_4$ on the anode and cathode sheets, respectively.

(shown in orange in the web version) and cathodes (shown in gray) form alternating layers with two cover sheets (shown in light blue). The separators (shown in white) are located between electrode and cover sheets. The cell RVE specimen is composed of 10 anode, 10 cathode, 21 separator and 2 cover sheets. The cell components were manually cut and assembled. The assembly of the cell components in the generic cell RVE specimen as schematically shown in Fig. 3(c) may be slightly different from those in usual lithium-ion cells for convenience of assembly of the purchased cell components. However, generic cell RVE specimens

with slightly different assemblies should have the similar buckling, kink and shear band mechanisms under constrained compression as discussed later due to their layered structures. The specimen has the size of 25 mm × 25 mm × 4.6 mm. No electrolyte was added for the dry cells. Due to the large specimen width in the X direction compared to the specimen thickness, the specimen width does not change before and after in-plane compression tests. Therefore, the specimens are subject to the plane strain conditions in the X direction under in-plane compression tests.
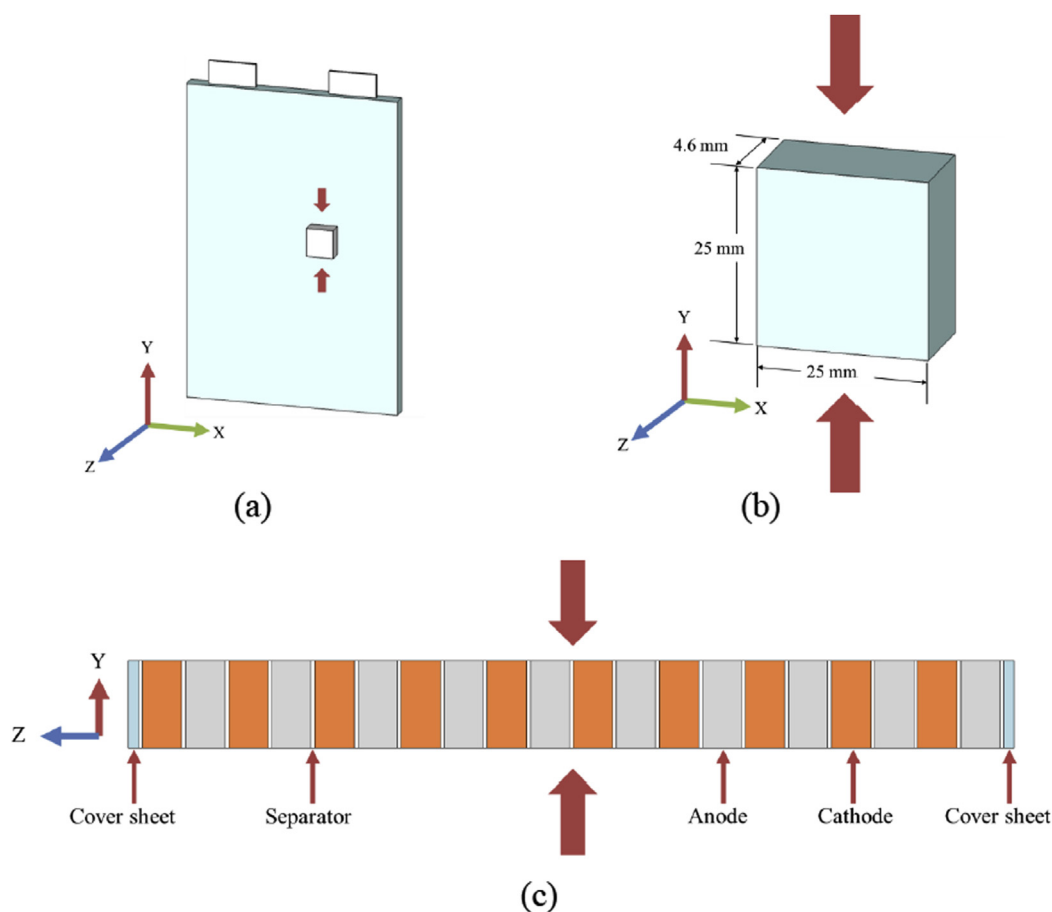
Fig. 3. A schematic of (a) a pouch cell and a cell RVE specimen for the in-plane constrained compression test, (b) a cell RVE specimen with the dimensions, and (c) a side view of a small portion of the cell RVE specimen showing the individual cell components. The large red arrows indicate the compressive direction. (For interpretation of the references to color in this figure legend, the reader is referred to the web version of this article.)

3. Quasi-static compression tests of cell RVE specimens

3.1. In-plane constrained compression tests of cell RVE specimens

Battery modules are usually held together by adhesive between the cells and the neighbor foam layers and aluminum heat dissipater sheets as well as two wrapping bands with tension. In the middle portion of a module, the cells are constrained by the neighbor foam layer and aluminum heat dissipater sheet. In an individual cell, the cell components can buckle individually with constraints from the neighbor cell components since there are no bonding forces between the cell components. Hence, a fully constrained die set was designed for constrained compression tests of cell RVE specimens. The punch and die setup for in-plane constrained compression tests of cell RVE specimens is shown in Fig. 4. The setup is composed of a male rectangular punch and a female die such that the specimen slot can be adjusted for different specimen geometries. A PMMA side window was made for recording the deformation process during the compression. The specimen slot in the die has an opening of 5 mm × 25 mm which leaves a gap of about 0.4 mm between the specimen and the side walls. The compression tests were conducted using a MTS Insight testing machine with a 10 kN load cell. The displacement rate is 0.5 mm min^{-1} (nominal strain rate of 0.0003 s^{-1}). The punch displacement was taken from the cross-head displacement recorded during the experiments.

Fig. 5 shows the nominal compressive stress–strain curves of three cell RVE specimens tested at a displacement rate of 0.5 mm min^{-1}. The specimens showed a nearly linear behavior in the beginning with the effective compressive elastic modulus of 188 MPa. The term "effective compressive elastic modulus" is used since the specimens are subjected to the plane strain conditions in the X direction. This value of 188 MPa is in good agreement with the effective compressive elastic modulus of 190 MPa which is estimated from the effective compressive elastic moduli of the nominal stress–strain curves of the cell component specimens under in-plane constrained compression tests based on the composite rule of mixture (ROM) presented in Appendix A. As shown in Fig. 5, a noticeable change of slope takes place when the strain increases to about 2%. As the strain continues to increase, the slope appears to remain constant until the strain reaches about 20%. Then the slope starts to increase gradually as the strain increases to about 34%. Some minor stress drops were observed after the initial linear stage due to the development of kinks and shear bands. The trends of all three curves are quite consistent. The nominal compressive stress–strain curve of the RVE specimen from the finite element analysis of Ali et al. [9] is also shown in Fig. 5 for comparison.

Fig. 6(a)–(d) show the deformation patterns of a cell RVE specimen at the nominal strain of 1% in the initial linear stage, at
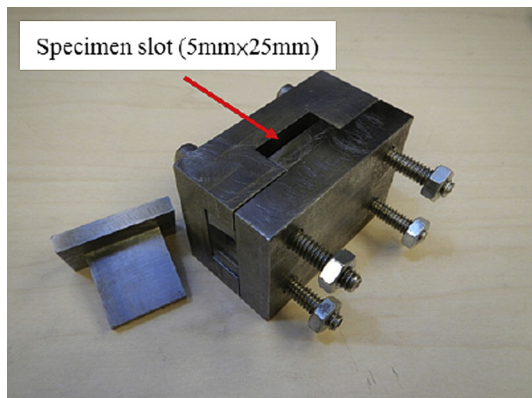

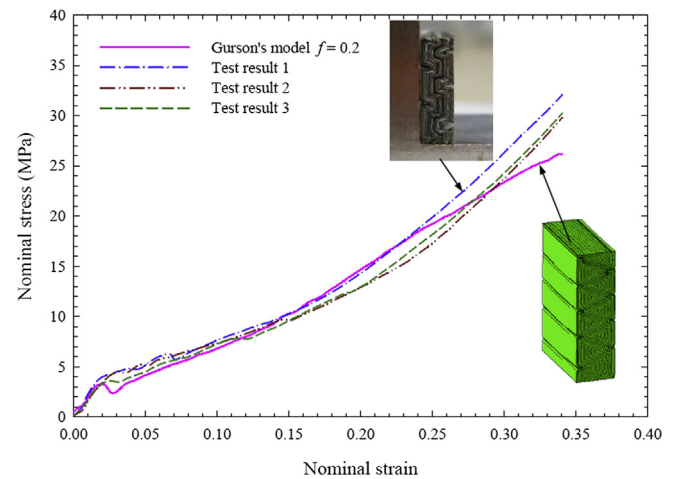**Fig. 4.** A punch and die setup for in-plane compression tests of cell RVE specimens.

Fig. 5. The in-plane nominal compressive stress–strain curves of three cell RVE specimens tested at a displacement rate of 0.5 mm min^{-1} (nominal strain rate of 0.0003 s^{-1}). The in-plane nominal compressive stress–strain curve of the cell RVE specimen from the finite element analysis using the Gurson's material model with a void volume fraction f set to 0.2 for the electrode and separator sheets is also shown for comparison.

the nominal strain of 2% where the slope changes, and at the nominal strains of 10% and 15%. A careful examination of the deformation pattern shown in Fig. 6(a) indicates the initial linear stage corresponds to the development of a smooth buckling mode of the cell components. A detailed analysis of the elastic buckling of the cell components will be presented in the next section. As the displacement increases toward the nominal strain of 2% where the slope starts to level off, the cell RVE specimen shows the development of kinks or plastic hinges of the cell components as indicated in Fig. 6(b). The presence of the kinks promotes the shear band formation as indicated in Fig. 6(b). The shear band formation creates a physical mechanism to efficiently accommodate for the in-plane compression and hence induces the slope change of the nominal stress–strain curve. As the strain continues to increase, more kinks and shear bands form across the cell RVE specimen, as shown in Fig. 6(c) and (d). Fig. 6(e) and (f) shows the front and back views of the tested cell RVE specimen at the nominal strain of about 34%. As shown in the figures, the kinks are fully developed to the folds and many shear band regions can be identified. After the efficient compaction mechanism of shear bands is completed, further compression can be accommodated by the micro buckling of the cell components outside the shear band regions, as marked in Fig. 6(e) and (f), and the compression in the shear band regions.

It should be noted that although the cell RVE specimen was almost fully constrained during the test, the clearance in the die between the specimen and the die walls in the out-of-plane direction still provided some space for the cell RVE specimen to buckle. Also, the large porosities of the graphite, LiFePO$_4$ and separator layers provided extra space for the components of the cell RVE specimen to buckle. In addition, the microscopic gaps between the cell components provided more space for the cell components to compact. As the displacement further increases in the last stage of compression, the cell RVE specimen reaches the nearly fully dense stage. At this stage, nearly 7 half waves of the macro buckling can be seen in Fig. 6(d)–(f). Based on the original specimen length, each half wavelength is about 3.6 mm, which is close to the specimen thickness (4.6 mm). The experimental results can also be compared with the results of the finite element analysis reported in Ali et al. [9]. As shown in Fig. 5, the nominal stress–strain curve from the finite element analysis based on the Gurson's yield function for the porous components of the cell specimen is in good agreement with the test results by selecting a
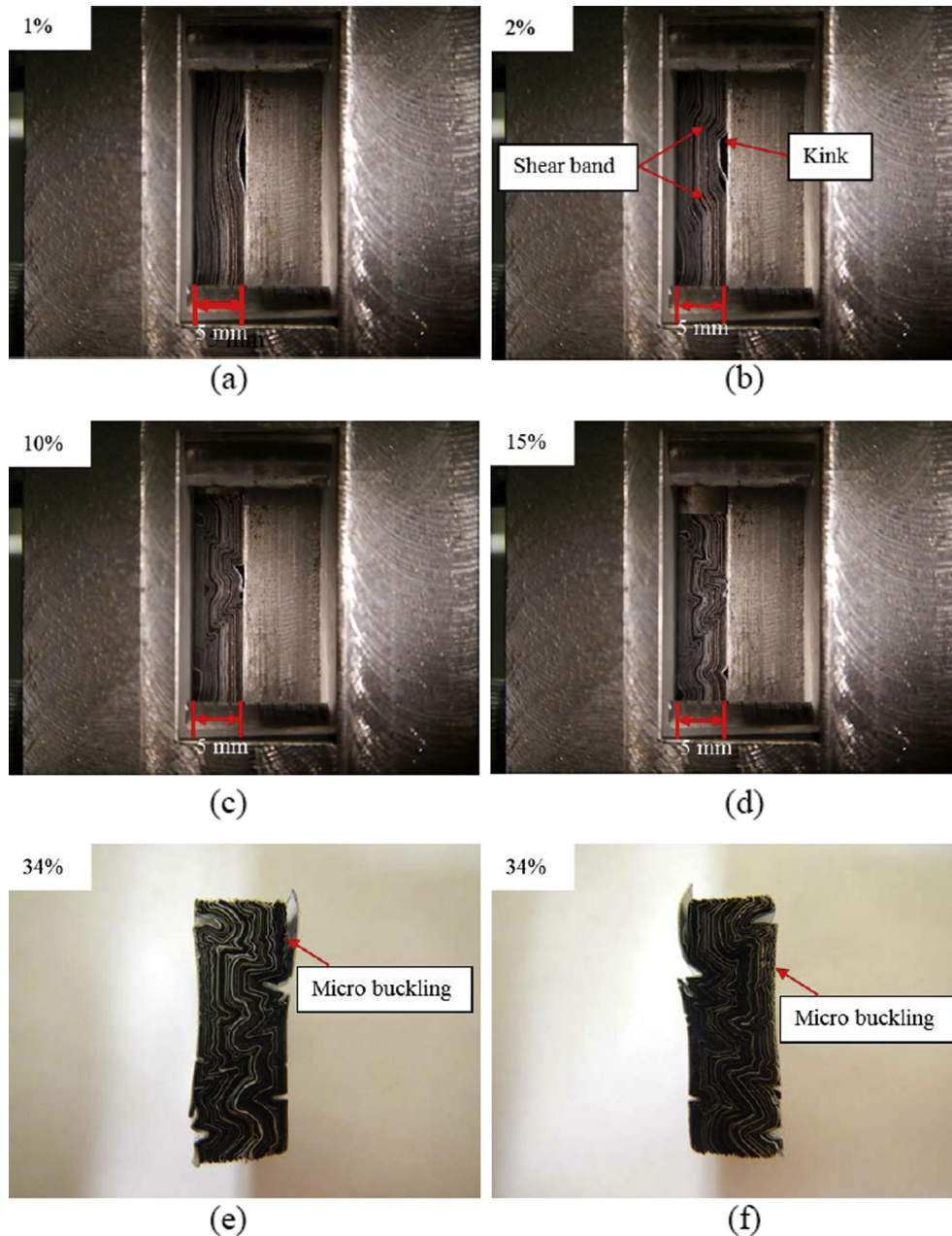
Fig. 6. Deformation patterns of a cell RVE specimen during the in-plane constrained compression test at the displacement rate of 0.5 mm min^{-1}: (a) at the nominal strain of 1% in the initial linear stage, (b) at the nominal strain of 2% where the slope change occurs, (c) at the nominal strain of 10%, (d) at the nominal strain of 15%, (e) at the nominal strain of 34% after the test (front view), and (f) at the nominal strain of 34% after the test (back view).

proper void volume fraction for the porous components of the cell RVE specimen. Images of the deformed cell at the strain of 34% from the experiment and the corresponding finite element analysis [9] are shown as two inserts in Fig. 5 for comparison. As shown in the figures, 7 half waves were observed in the experiment whereas 10 half waves were obtained from the finite element analysis.

As indicated in Sahraei et al. [5], cutting specimens from commercial full sized battery cells poses a formidable task. Testing high voltage automotive battery cells and modules is expensive and needs special safety attention since electrolyte is toxic and difficult to handle. The results of a companion research program on testing full sized commercial battery cells under in-plane constrained compression at Sandia Battery Abuse Testing Laboratory showed similar stress–strain curves as those presented in this paper. However, with the severe thermal event for the full sized commercial

battery cells under compression, it was difficult to observe and understand the fundamental deformation mechanisms of the battery cells under compression. The compressive stress–strain curves of small lithium cobalt dioxide cells for cell phones presented in Sahraei et al. [5] are also similar to those presented in this paper. It should be noted that one focus of this paper is on characterizing and understanding the compressive behavior of cells rather than characterizing specific battery cells, with or without electrolyte, which may vary from one manufacturer to another.

3.2. Out-of-plane compression tests of cell RVE specimens

Fig. 7(a) shows a schematic of a pouch cell and a cell RVE specimen with the X–Y–Z coordinate system. A small out-of-plane compression cell RVE specimen is shown in Fig. 7(b) with the
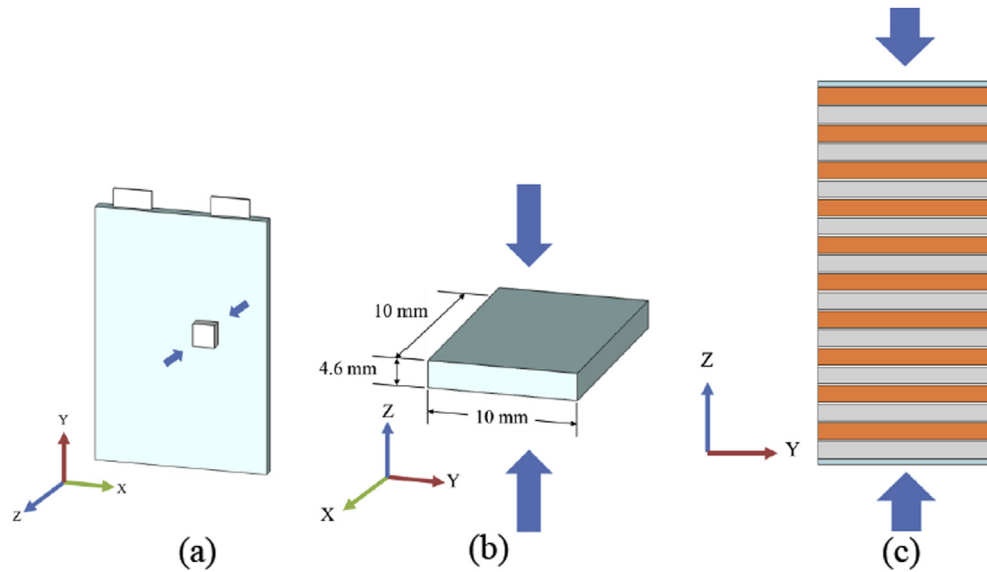
Fig. 7. A schematic of (a) a pouch cell and a cell RVE specimen for the out-of-plane compression test, (b) a cell RVE specimen with the dimensions, and (c) a side view of a small portion of the cell RVE specimen showing the individual cell components. The large blue arrows indicate the compressive direction. (For interpretation of the references to color in this figure legend, the reader is referred to the web version of this article.)

dimensions. Fig. 7(c) shows a side view of a small portion of the cell RVE specimen with the individual cell components. The large blue arrows shown in the figure indicate the out-of-plane compressive direction. The out-of-plane compression cell RVE specimen was smaller than the in-plane compression cell RVE specimen in order to avoid exceeding the load limit of the load cell. The size of the out-of-plane compression cell RVE specimen is reduced to 10 mm × 10 mm × 4.6 mm as shown in Fig. 7(b). The layered structure of the cell RVE specimen is the same as that of the cell RVE specimens for in-plane constrained compression tests. The test was conducted using a MTS Insight testing machine with a displacement rate of 0.25 mm min^{-1} (nominal strain rate of 0.0009 s^{-1}). No constraint was applied to the lateral sides of the specimen in the X and Y directions.

Three nominal compressive stress–strain curves of the cell RVE specimens under out-of-plane compression are shown in Fig. 8(a). The three in-plane nominal compressive stress–strain curves in Fig. 5 are also shown for comparison. As shown in the

figure, the low stress response in the early stage of the out-of-plane compression tests can be attributed to the consumption of the porosity in the cell components and the microscopic gaps between the cell components. With the increasing strain, densification of the cell components kicked in and contributed to the sharp increase of the stress. The nominal stress–strain curves appear to be linear elastic again at the strain of about 40% as the strain increases. This suggests that the total volume fraction of the porosity in the components and the microscopic gaps between the components is about 40% when the cell RVE specimens are nearly fully condensed and become linear elastic as the strain increases. The tested specimens retained the final thicknesses and appeared to be permanently deformed. However, no dimension change was observed in the two lateral directions perpendicular to the loading direction, which corresponds to zero Poisson's ratio. Fig. 8(b) shows pictures of cell RVE specimens before (left) and after (right) the compression.
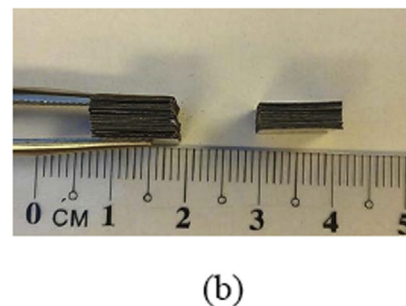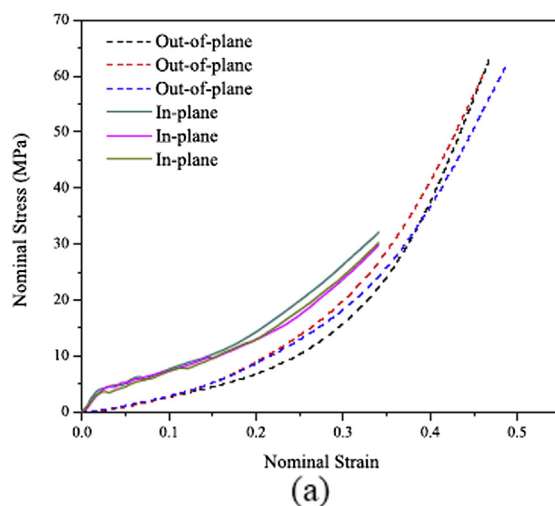
Fig. 8. (a) The out-of-plane nominal compressive stress–strain curves of cell RVE specimens tested at a displacement rate of 0.25 mm min^{-1} (nominal strain rate of 0.0009 s^{-1}) and (b) pictures of two specimens before (left) and after (right) compression. The three in-plane nominal compressive stress–strain curves as shown in Fig. 5 are also shown in (a) for comparison.

4. Buckling analyses of cell RVE specimens under in-plane constrained compression

Based on the experimental observations of the cell RVE specimens under in-plane constrained compression, the physical mechanism to accommodate the compression starts with the elastic buckling of the cell components. When a cell RVE specimen was made, the component sheets were first assembled and packed together. The specimen was then put in the slot of the female die. When a cell RVE specimen is under in-plane compression, the component sheets buckle independently with the lateral constraints from the neighbor component sheets. Since the component sheets were only packed together, each component sheet can be treated as an individual thin plate or beam under in-plane compression with the lateral constraints which can be treated as unattached elastic foundations.

Fig. 9 shows a uniform straight beam under end loads and supported by two unattached elastic foundations. Both ends are hinged and the beam is supported by the elastic foundations through the lateral pressure proportional to the deflection in the Z direction. Here, and represent the spring constants of the harder and softer elastic foundations on the two sides of the beam, respectively. The buckling load solution of the beam can be found in Ref. [11]. Based on the solution listed in Ref. [11], the buckling load of the i-th component with the two unattached elastic foundations can be expressed as

$$P_m^i = \frac{m^2\pi^2 E_i' I_i}{L^2} + \frac{k_2 L^2}{m^2 \pi^2}\phi^\alpha \tag{1}$$

where m represents the number of half waves in which the component buckles and is equal to the lowest integer greater than $\overline{m}$. Here, $\overline{m}$ is defined as

$$\overline{m} = \frac{1}{2}\left(\sqrt{1 + \frac{4L^2}{\pi^2}\sqrt{\frac{k_2}{E_i' I_i}}} - 1\right) \tag{2}$$

In Equation (1), $\phi = k_1/k_2$ and α depends upon the value of m. In Equations (1) and (2), $I_i \,(= bh_i^3/12)$ is the moment of inertia for the i-th component. E_i' is the effective elastic modulus for a thin plate under plane strain compression conditions and is equal to $E_i/(1 - \nu_i^2)$, where E_i and ν_i are the compressive elastic modulus and Poisson's ratio of the i-th component. The effective compressive elastic moduli for the cell component specimens are listed in Table 2. Here, L, b and h_i are the length, width, and thickness of the i-th component.

As suggested from the experimental observations and the results reported in the finite element analysis [9], the cell components buckle first. After the buckling of the cell components, kinks and shear bands are formed according to the buckling mode of the cell components. Based on the experimental observations, the cell RVE specimens appear to buckle in an asymmetric fashion where no symmetry with respect to the central anode sheet was observed. However, the results of the finite element analysis [9] indicated that in the very early stage the component sheets buckle in the symmetric mode. For anode, cathode, and separator sheets in the cell RVE specimen, the sheets can be thought as a beam with two unattached elastic foundations on both sides. For the anode, cathode and separator sheets in the middle portion of the cell RVE specimens, the buckling mode will be dominated by the constraints on both sides of the sheets. It is assumed that the spring constants for the elastic unattached foundations are the same and denoted by k. Here, k represents the lateral force per unit plate length per unit deflection of the neighbor components in the out-of-plane direction. The spring constant k can be expressed in terms of the out-of-plane compressive elastic modulus E of the cell RVE specimens as
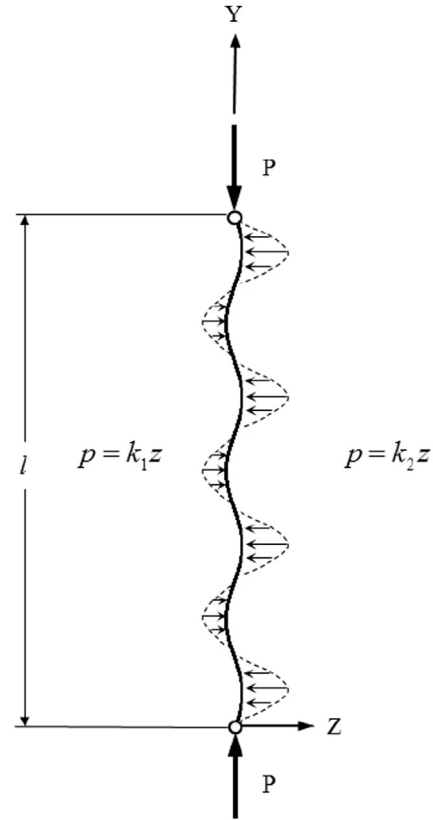

Fig. 9. A schematic of a uniform straight beam under end loads and supported by unattached elastic foundations. Both ends are hinged and the beam is supported by the elastic foundations through the lateral pressure p proportional to the deflection in the Z direction. The elastic foundations on two sides of the beam have the spring constants k_1 and k_2.

$$k = \frac{Eb}{h} \tag{3}$$

where h represents the thickness of the neighbor cell components. With the elastic spring constant k on both sides of the beam is equal to each other, Equation (1) becomes

$$P_m^i = \frac{m^2\pi^2 E_i' I_i}{L^2} + \frac{kL^2}{m^2\pi^2} \tag{4}$$

where m again represents the number of half waves in which the component buckles and is equal to the lowest integer greater than $\overline{m}$ as before. Here, $\overline{m}$ is defined as

$$\overline{m} = \frac{1}{2}\left(\sqrt{1 + \frac{4L^2}{\pi^2}\sqrt{\frac{k}{E_i' I_i}}} - 1\right) \tag{5}$$

Equations (4) and (5) represent the buckling solution in Timoshenko [12] for a beam with an attached elastic foundation. Considering m as a real number as in Ali et al. [9], $\partial P_m^i/\partial m = 0$ gives

Table 2
Effective compressive elastic moduli of cell components.

	Effective compressive elastic modulus (MPa)
Cover sheet	575
Anode	83
Cathode	275
Separator	90

$$m = \left(\frac{k}{E_i'I_i}\right)^{\frac{1}{4}}\frac{L}{\pi} \tag{6}$$

The critical buckling load P_c^i can be determined as

$$P_c^i = 2(kEI)^{\frac{1}{2}} \tag{7}$$

Equation (6) can be rewritten for the half wavelength L m^{-1} as

$$\frac{L}{m} = \left(\frac{E_i'I_i}{k}\right)^{\frac{1}{4}}\pi \tag{8}$$

As indicated in Equations (7) and (8), the critical buckling load P_c^i and the half wavelength L m^{-1} are independent of the specimen length.

The cover sheets have only one unattached elastic foundation and are free to buckle to the unconstrained side due to the small clearances in the die for the cell RVE specimen. However, the small clearances will limit the cover sheets to fully develop a lower order buckling mode. For the anode, cathode and separator sheets near the cover sheets, they can start to buckle in a lower order mode but will also be constrained by the rigid walls through the cover sheets. The results of the finite element analysis [9] indicate that the cover sheets are constrained by the rigid walls and buckle in a high order mode. For a beam with one unattached elastic foundation on one side and a small clearance to a rigid wall on the other side, the elastic buckling solution is approximated by the elastic buckling solution for a beam with an unattached elastic foundation on one side and a rigid wall on the other side as discussed in Ali et al. [9]. For the cover sheets and the neighbor sheets, the buckling load of the i-th component can approximately be expressed as

$$P_n^i = \frac{4n^2\pi^2E_i'I_i}{L^2} + \frac{3kL^2}{4n^2\pi^2} \tag{9}$$

where n represents the number of waves in which the component buckles and is equal to the lowest integer greater than $\overline{n}$. Here, $\overline{n}$ is defined as

$$\overline{n} = \frac{1}{2}\left(\sqrt{1 + \frac{4L^2}{\pi^2}\sqrt{\frac{3k}{16E_i'I_i}}} - 1\right) \tag{10}$$

Considering n as a real number as in Ali et al. [9], $\partial P_n^i/\partial n = 0$ gives

$$n = \left(\frac{3k}{16E_i'I_i}\right)^{\frac{1}{4}}\frac{L}{\pi} \tag{11}$$

The critical buckling load P_c^i can be determined as

$$P_c^i = 2\sqrt{3}\left(kE_i'I_i\right)^{\frac{1}{2}} \tag{12}$$

Equation (11) can be rewritten for the wavelength L/n as

$$\frac{L}{n} = \left(\frac{16E_i'I_i}{3k}\right)^{\frac{1}{4}}\pi \tag{13}$$

As indicated in Equations (12) and (13), the critical buckling load P_c^i and the wavelength L/n are independent of the specimen length.

The elastic compressive modulus E of the cell obtained from the out-of-plane compression tests of the cell RVE specimens is 8.5 MPa. The spring constant k can be estimated as 4.6×10^7 N m^{-2} for the cover sheets and neighbor sheets near the die walls, and 9.2×10^7 N m^{-2} for the component sheets in the middle portion of the cell specimen. For the sheets in the middle portion of the cell specimen, the original solution given by Timoshenko [12] in Equations (4) and (5) can be used

Table 3
Buckling modes, loads, and strains for the component sheets in the middle portion of the cell RVE specimen with $k = 9.2 \times 10^7$ N m^{-2} and buckling loads and stresses for the cell RVE specimen.

	Cover sheet	Anode	Cathode	Separator
$\overline{m}$	21.3 (NA)	22.2	16.3	124.6
P_m^i (N)	25.3 (NA)	23.3	42.7	0.744
ε_m^i	0.0159 (NA)	0.0562	0.0310	0.0165
Cell buckling load P_{cell} (N) at the component buckling strain ε_m^i	350 (NA)	1240	684	364
Cell buckling stress σ_{cell} (MPa) at the component buckling strain ε_m^i	2.80 (NA)	9.90	5.47	2.91

to estimate the buckling modes and loads of the component sheets in the middle portion of the specimen as listed in Table 3. The results for the cover sheets are not applicable (NA) but are listed in Table 3 for reference only. As listed in Table 3, the values for $\overline{m}$ are 21.3, 22.2, 16.3 and 124.6 based on Equation (5) which give the buckling modes of 22, 23, 17 and 125 that give the lowest buckling loads with the constraints for the cover sheet, anode, cathode and separator sheets in the middle portion of the cell specimen, respectively.

For the cover sheets and the neighbor sheets near the die walls, the buckling modes and loads can be estimated based on Equations (9) and (10) for a beam with an unattached elastic foundation on one side and a rigid boundary on the other side as listed in Table 4. Note that one wave of the cover sheets and neighbor sheets corresponds to two half waves of the component sheets in the middle portion of the cell RVE specimen. Therefore, the values for $2\overline{n}$ are listed in Table 4 for comparison. As listed in Table 4, the values for $2\overline{n}$ are 23.1, 24.1, 17.6 and 137.4, which give the buckling mode number $2n$ of 24, 26, 18 and 138 that give the lowest buckling loads with the constraints for the cover sheet, anode, cathode and separator sheets near the sides of the cell RVE specimen, respectively. The corresponding buckling loads for the component sheets are listed in Tables 3 and 4.

The corresponding compressive strains at these buckling loads can be calculated by

$$\varepsilon_m^i = \frac{P_m^i}{E_i'A_i} \quad \text{or} \quad \varepsilon_n^i = \frac{P_n^i}{E_i'A_i} \tag{14}$$

for the component sheets in the middle portion or near the sides of the cell specimen. Here, is the cross sectional area of the i-th component. Equation (14) gives the strains at these buckling loads for the i-th components. The values are also listed in Tables 3 and 4. As listed in the tables, the strains for all the cell components calculated in both buckling analyses are comparable to those obtained from the experiments and from the results of the finite element analysis [9].

Table 4
Buckling modes, loads, and strains for the component sheets near the sides of the cell RVE specimen with $k = 4.6 \times 10^7$ N m^{-2} and buckling loads and stresses for the cell RVE specimen.

	Cover sheet	Anode	Cathode	Separator
$2\overline{n}$ (for comparison with those in Table 3)	23.1	24.1	17.6	137.4
P_n^i (N)	30.1	27.7	50.5	0.908
ε_n^i	0.0189	0.0666	0.0367	0.0202
Cell buckling load P_{cell} (N) at the component buckling strain ε_n^i	416	1470	809	445
Cell buckling stress σ_{cell} (MPa) at the component buckling strain ε_n^i	3.33	11.7	6.47	3.56

The buckling loads of the cell RVE specimen when the cell components buckle can be obtained by summing over the loads of the cell components at the strains when the cell components buckle as

$$P_{\text{cell}} = \varepsilon_m^i \sum n_i E_i' A_i \ \text{ or } \ P_{\text{cell}} = \varepsilon_n^i \sum n_i E_i' A_i \tag{15}$$

where n_i is the number of the i-th component in the cell RVE specimen according to the composite rule of mixture. The nominal buckling stress of the cell RVE specimen can be obtained by dividing the load by the cross sectional area of the cell RVE specimen as

$$\sigma_{\text{cell}} = \frac{P_{\text{cell}}}{A} \tag{16}$$

The buckling stresses for the cell RVE specimen based on the buckling loads of the cover sheets, anode, cathode and separator sheets near the sides of the cell RVE specimen are 3.33, 11.7, 6.47, and 3.56 MPa as listed in Table 4. It should be noted that the results of the finite element analysis in Ref. [9] suggest that the cover sheets actually buckle first. The buckling stress of 3.33 MPa based on the buckling load of the cover sheets near the sides of the cell RVE specimen in Table 4 in general agrees with the critical stress of 4.0 MPa obtained from the experiments. The buckling stresses for the cell RVE specimen based on the buckling loads of the anode, cathode and separator sheets in the middle portion of the cell RVE specimen are 9.90, 5.47, and 2.91 MPa as listed in Table 3. The buckling stresses listed in Tables 3 and 4 in general agree with the critical stress of 4.0 MPa obtained from the experiments.

It should be noted again that the results of the finite element analysis in Ref. [9] suggest that the cover sheets actually buckle first. Based on Equation (10), $\bar{n} = 11.62$ and $n = 12$ for the cover sheets. This corresponds to 24 half waves for the cell RVE specimen. Note that 7 half waves were observed in the experiment whereas 10 half waves are obtained from the corresponding finite element analysis [9]. However, the in-plane constrained compression test conducted in this investigation has a total clearance of 0.358 mm between the cell RVE specimen and the die walls. This can reduce the spring constants for the unattached elastic foundations. The computational results indicate that when the clearance is reduced to 0, 15 half waves appear which is reasonably in agreement with about 20 half waves obtained by both elastic buckling analyses. It should be noted that the analytical results based on Equations (5) and (10) are approximate in nature and the analytical results are in reasonable agreement with the experimental and computational results.

As indicated in Equations (8) and (13), the half wavelength L m^{-1} for the component sheets in the middle portion of the cell RVE specimens and the wavelength L/n for the component sheets near the sides of the cell RVE specimens are independent of the specimen length. As indicated in Equations (7) and (12), the buckling loads are functions of the elastic bending rigidity and the out-of-plane elastic modulus of the cell RVE specimens, and they are independent of the specimen length. The results suggest that the length of the cell RVE specimens is appropriately selected since the cell RVE specimens buckle with multiple half waves under in-plane constrained compression. Therefore, the constrained compressive behavior of the cell RVE specimens obtained in this investigation can in general represent that of battery cells with a full length. After the buckling mode is settled, plastic hinges or kinks will develop and the shear band mechanism will kick in to efficiently compact the cell RVE specimens as the compression continues.

5. Kink and shear band formation under in-plane constrained compression

Based on the experimental observations of the cell RVE specimens under in-plane constrained compression, the physical mechanism to accommodate the compression can be summarized in the following. First, the elastic buckling of the cell RVE components takes place. Next, kinks of the components are initiated and consequently shear band regions across the specimen are formed. As the compression continues, the shear band regions are compressed, sheared and rotated. Also, the regions outside the shear bands are under compression. Once the shear band regions reach their shear and rotational limits, compaction takes place in both regions inside and outside of the shear bands.

Fig. 10(a)–(f) shows an idealized deformation process in a cell RVE specimen under in-plane constrained compression without any clearance between the specimen and the die walls to explain the kink and shear band formation mechanism in the specimen and estimate the strains inside and outside of the shear band region in terms of the kink length, kink angle and shear band angle. Fig. 10(a)–(c) shows schematics of a cell RVE specimen before, during, and after the formation of shear band regions under in-plane constrained compression, respectively. Fig. 10(d)–(f) shows the detailed schematics of one unit cell of the specimen corresponding to Fig. 10(a)–(c), respectively. Fig. 10(a) and (d) shows the original configuration of the specimen before the kinks and shear band regions are formed. In Fig. 10(a), region I between two parallel dashed lines as marked represents the shear band region. Since no shear bands are formed, the initial kinked angle α (as marked in Fig. 10(e) is 90°. Fig. 10(b) and (e) shows the configuration where the kinks are formed and the shear band regions are compressed, sheared and rotated. During the deformation process, the kinked angle α decreases from the original kink angle of $\alpha = 90°$ to the final kink angle of $\alpha = 0°$. Fig. 10(c) and (f) shows the configuration when the shear band region has reached its shear and rotational limit.

Fig. 10(d)–(f) shows the deformation history of one unit cell of the specimen. In Fig. 10(d), the global Y and Z coordinates are shown. In Fig. 10(d)–(f), the local material Y' and Z' coordinates represent the coordinates that rotate or move with the material during the deformation. In Fig. 10(d)–(f), w represents the cell thickness, d represents the kink length (which is assumed to be constant in this idealized model), θ represents the shear band angle, and θ_i and θ_f represent the initial and final shear band angles, respectively. As shown in Fig. 10(d), shear bands (between two parallel dashed lines) are to be formed across the cell RVE specimen (shown in gray) to accommodate the compression. During the deformation, the kink angle α deceases from 90° toward 0° while the shear band angle changes due to the rotation of the shear band region and the deformation in the regions inside and outside the shear band. As shown in Fig. 10(d)–(f), the shear band region I can be represented by the parallelogram ABCD which is deformed into A′B′C′D′ and then A″B″C″D″. Therefore, in region I inside the shear band, the material has the compressive strains in the Y' and Z' directions and the shear strain in the $Y'-Z'$ plane. As shown in Fig. 10(d)–(f), region II outside the shear band can be represented by the triangle CDE which is deformed into C′D′E′ and then C″D″E″. Therefore, in region II outside the shear band, the material is under biaxial compressive strains in the Y' and Z' directions. After reaches 0°, θ decreases as the compression continues. It should be noted that Fig. 10(a)–(f) are idealized. In reality, the shear bands do not form at the same time and the shear band angles are different for different parts of the specimens.

Based on the idealized shear band deformation process, the local material strains inside and outside the shear band regions can be estimated in terms of the compressive strain of the cell RVE specimen. The shear band mechanism appears to optimize the total compressive strain in the Y direction. It should be mentioned that the cell can be thought of a unidirectional composite where the load carrying capacity is high in the Y or Y' direction and low in the Z or Z' direction under compression. Therefore, the strain in the Y' direction is assumed to be zero in the shear band region for this
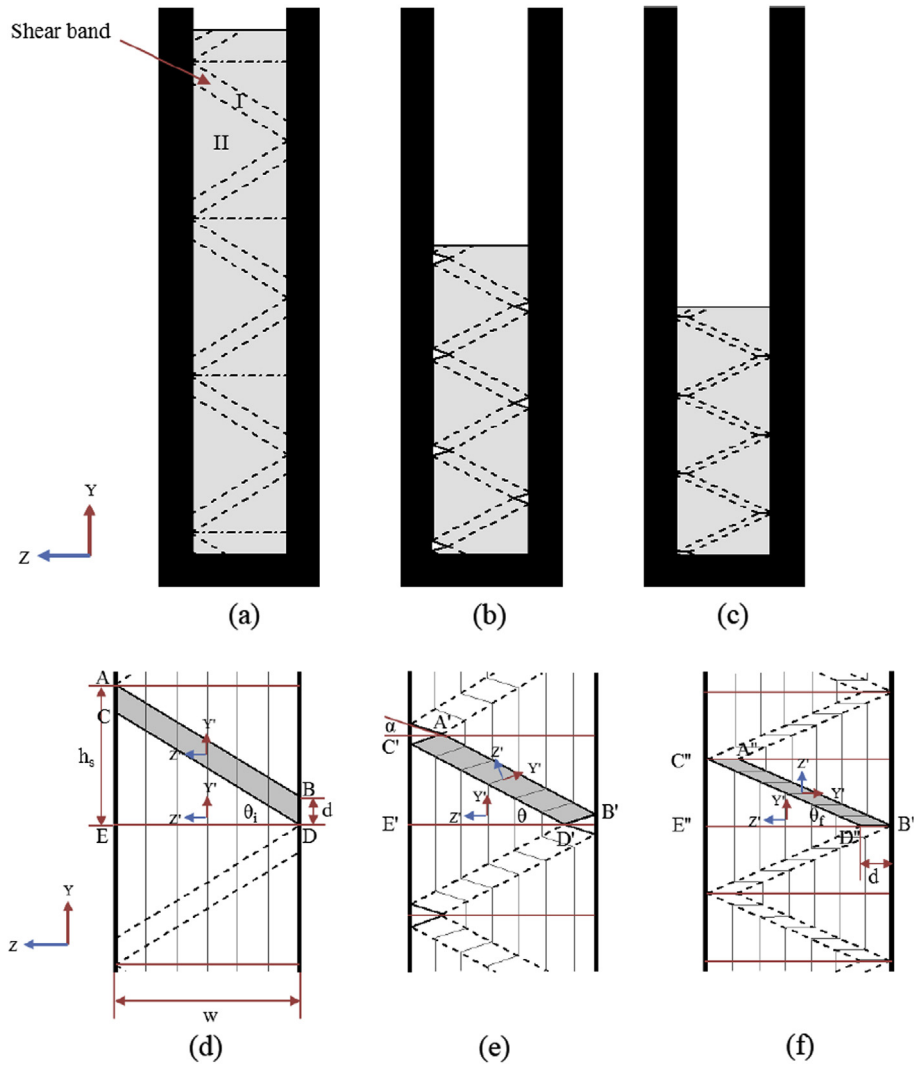
Fig. 10. Schematics of a cell RVE specimen (a) before, (b) during, and (c) after the shear band formation. (d)–(f) are detailed schematics corresponding to (a)–(c), respectively. The Y and Z coordinates are the global coordinates and the Y' and Z' coordinates are the local material coordinates in (d)–(f).

idealized model. The nominal strains in region I inside the shear band with respect to the local material coordinate system are

$$\varepsilon_{Y'} = 0 \tag{17}$$

$$\varepsilon_{Z'} = \frac{\left(\frac{w - d\cos\alpha}{\cos\theta}\right)\sin(\alpha + \theta) - w}{w} \tag{18}$$

$$\gamma_{Y'Z'} = \frac{\pi}{2} - \alpha - \theta + \tan^{-1}\left(\frac{(w - d\cos\alpha)\tan\theta}{w}\right) \tag{19}$$

Here, the engineering shear strain $\gamma_{Y'Z'}$ is defined according to the definition of the engineering shear strain of the small strain theory. The nominal strains in region II outside the shear band with respect to the local coordinate system can be expressed as

$$\varepsilon_{Y'} = \frac{(w - d\cos\alpha)\tan\theta - w\tan\theta_i}{w\tan\theta_i} \tag{20}$$

$$\varepsilon_{Z'} = \frac{(w - d\cos\alpha) - w}{w} = \frac{-d\cos\alpha}{w} \tag{21}$$

The total nominal strain ε_Y^T for one unit cell of the specimen can be written as

$$\varepsilon_Y^T = \frac{\Delta h_s}{h_s} = \frac{[(w - d\cos\alpha)\tan\theta + d\sin\alpha] - (w\tan\theta_i + d)}{w\tan\theta_i + d} \tag{22}$$

where h_s is the shear band height. The nominal strains inside and outside the shear band can be estimated for a given set of w, d, θ_i, and θ.

When the compressive strain in the Y' direction in region II increases uniformly, the shear band angle remain unchanged. Since the change of the shear band angle θ was found to be small as α decreases, the shear band angle is assumed to be constant. With this assumption, the equations for the nominal strains in both regions can be simplified. For region I inside the shear band region, Equation (18) can be simplified to

$$\varepsilon_{Z'} = \frac{\left(\frac{w - d\cos\alpha}{\cos\theta_i}\right)\sin(\alpha + \theta_i) - w}{w} \tag{23}$$

In region II outside of the shear band region, Equation (20) can be simplified to

$$\varepsilon_{Y'} = \frac{-d\cos\alpha}{w} \tag{24}$$

Equations (21) and (24) indicate that region II is now subjected to equal biaxial compression. The total nominal strain for one unit cell of the specimen in Equation (22) can be simplified to

$$\varepsilon_Y^T = \frac{-d\cos\alpha\tan\theta_i + d\sin\alpha - d}{w\tan\theta_i + d} \tag{25}$$

The nominal strains inside and outside the shear band region can be estimated for $\alpha = 0$ when the shear band reaches its shear and rotational limit. The total nominal strain in Equation (25) becomes

$$\varepsilon_Y^T = \frac{-d\tan\theta_i - d}{w\tan\theta_i + d} = \frac{-\frac{d}{w}(\tan\theta_i + 1)}{\tan\theta_i + \frac{d}{w}} \tag{26}$$

As indicated in Equation (26), the shear band compaction mechanism is quite efficient to produce compaction with the extra contribution due to the kink length d. After α reaches the limit of 0, the shear band angle θ decreases as the compression increases in both regions I and II.

Another idealization can also be made with the assumption that the cell components are rigid in the Y or Y' direction but plastic hinges or kinks can be formed whereas the components are compliant in the Z or Z' direction. In this case, the nominal strain in the Y or Y' direction in region II becomes

$$\varepsilon_{Y'} = 0 \tag{27}$$

The additional term due to the compressive strain in the Y or Y' direction in region II in Equation (26) disappears and the total strain of one unit cell of the specimen becomes

$$\varepsilon_Y^T = \frac{-d}{w\tan\theta_i + d} = \frac{-\frac{d}{w}}{\tan\theta_i + \frac{d}{w}} \tag{28}$$

As indicated in Equation (28), the total compressive strain of the specimen can be estimated easily from the normalized kinked length d/w. Finally, it should be mentioned that the deformation mechanism as discussed here is purely kinematic and it gives some physical insight on the deformation mechanism of the cell RVE specimens under in-plane constrained compression as observed in experiments and as obtained from the results of the finite element analysis [9].

It should be mentioned that the physical mechanism of the kink and shear band formation appears in different types of battery cells such as the lithium iron phosphate battery RVE specimens under in-plane constrained compression as investigated in this paper and the lithium cobalt dioxide battery cells under in-plane constrained compression as reported in Ref. [5]. The physical mechanism also appears in cover sheet, anode, cathode and separator specimens as shown in Figs. A1–A4. Note that the anode, cathode and separator are compressible porous sheets while the cover sheet is made of nearly incompressible polyamide, polypropylene and adhesives. It seems that the physical mechanism of the kink and shear band formation is a general deformation mechanism that can appear in unattached sheets under in-plane constrained compression.

6. Conclusions

In this study, the mechanical behavior of cell RVE specimens was investigated under both in-plane constrained and out-of-plane compressive loading conditions. The designs of the cell RVE specimens and the in-plane constrained compression test setup are for cells in the middle portion of a module with the lateral constraints in the out-of-plane direction. For this investigation, conclusions can be made in the following.

1. Quasi-static in-plane constrained compression tests of cell RVE specimens were conducted. The deformation process is correlated to the nominal stress–strain curve by carefully examining the recorded deformation patterns and the stress–strain curves concurrently. The results indicate the load carrying behavior of cell RVE specimens is characterized by the buckling of cells with a wavelength approximately in the order of the thickness of the cells, kink and shear band formation, and the final densification of the cell components.
2. The nominal compressive stress–strain curves of cell RVE specimens under in-plane constrained and out-of-plane compression are different. The different nominal compressive stress–strain curves in the in-plane and out-of-plane directions suggest that the cells can be modeled as anisotropic foams or cellular materials. The in-plane and out-of-plane nominal compressive stress–strain curves presented in this paper can be used to develop macro homogenized anisotropic material models for crashworthiness analyses.
3. The initial elastic buckling mode of the cell RVE specimen under in-plane constrained compression can be correlated to the elastic buckling solution of a beam with lateral constraints. The development of the higher order buckling modes of the component sheets and the critical stresses observed in experiments are in agreement with the results of the analytical buckling solutions and the corresponding finite element analyses. The elastic buckling analyses also justify the length selection of the cell RVE specimens.
4. An idealized kinematic model is developed to explain the kink and shear band formation in the cell RVE specimens under in-plane constrained compression. The nominal strains in the regions inside and outside of the shear band can be estimated by the idealized model and the results give some insight on the physical deformation process observed in experiments. The kinematic model appears to be valid in general for unattached sheets under in-plane constrained compression.

Appendix A. Effective compressive elastic moduli of cell components under in-plane constrained compression

In-plane constrained compression tests were conducted for the component sheets to examine the deformation patterns and to estimate the effective compressive elastic moduli of the component sheets. These effective compressive elastic moduli are then used to estimate the effective compressive elastic modulus of the cell RVE specimens based on the composite ROM and compared to the value obtained from the test results of the cell RVE specimens under in-plane constrained compression

tests. The specimens of cell components were made by stacking different numbers of sheets of cell components to a total thickness of 5 mm. The specimens have the in-plane dimensions of 25 mm × 25 mm. The numbers of sheets for the cover sheet, anode, cathode, and separator specimens are 45, 25, 25, and 250, respectively, to make the total specimen thickness of 5 mm. The test procedure is the same as stated in Section 3.1.

Fig. A1(a) shows the nominal stress–strain curves of cover sheet specimens. The effective compressive elastic modulus is estimated by taking a linear fitting curve for the beginning part of the curve. The fitting curve is indicated by a red dashed line shown in the figure. The estimated effective compressive elastic modulus is about 575 MPa. Estimations of the effective compressive elastic moduli for all component specimens follow the same procedure. Fig. A1(b)–(d) shows the deformation patterns of a cover sheet specimen at different nominal strains. The deformation patterns are similar to those of the cell RVE specimens.

Fig. A2(a) shows the nominal stress–strain curves of anode specimens. The estimated value of the effective compressive elastic modulus is about 90 MPa. Fig. A2(b)–(d) shows the deformation patterns of an anode specimen at different nominal strains. It is noted that the deformation patterns are similar to those of the cell RVE specimens.

Fig. A3(a) shows the nominal stress–strain curve of a cathode specimen. The estimated effective compressive elastic modulus is about 275 MPa. Fig. A3(b)–(d) shows the deformation patterns of the cathode specimen at different nominal strains. The deformation patterns are similar to those of the cell RVE specimens in the

beginning of the test. As the strain increases, the deformation pattern deviates from those of the cell RVE specimens.

Fig. A4(a) shows the nominal stress–strain curves of separator specimens. The estimated effective compressive elastic modulus is about 83 MPa. Fig. A4 (b)–(d) shows the deformation patterns of a separator specimen at different nominal strains. The deformation patterns show a much shorter wavelength compared to those of the cell RVE specimens. The effective compressive elastic moduli for the cell component specimens are listed in Table 2.

The composite ROM is used to estimate the effective compressive elastic modulus of the cell RVE specimen based on the effective compressive elastic moduli of the component sheet specimens. The effective compressive elastic modulus of the cell RVE specimen, E'_{cell}, can be estimated as

$$E'_{cell} = \sum f_i E'_i \tag{A1}$$

where f_i and E'_i are the volume fraction and the effective compressive elastic modulus of the i-th cell component. The estimated E'_{cell} is 190 MPa, which is close to the effective compressive elastic modulus of 188 MPa obtained from the test results of the cell RVE specimens under in-plane constrained compression tests. The effective compressive elastic moduli of the cell component specimens are then used for the input for the elastic buckling analysis of the cell components in this investigation, the simulations of the deformation process of the cell RVE specimens [9], and the elastic buckling analysis of the module RVE specimens [8].
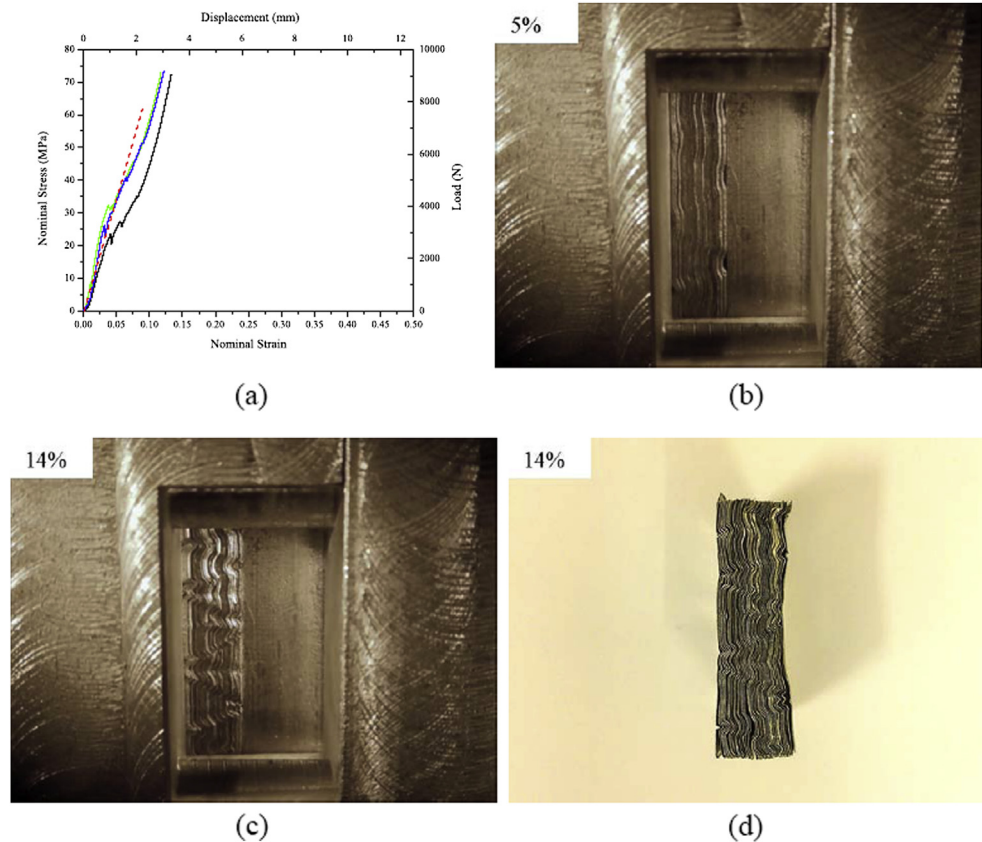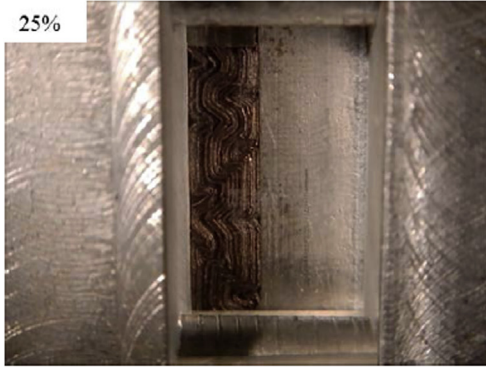

Fig. A1. (a) The in-plane nominal compressive stress–strain curves of cover sheet specimens tested at a displacement rate of 0.5 mm min^{-1} (nominal strain rate of 0.0003 s^{-1}). (b–d) show the deformation patterns of a cover sheet specimen at the nominal strains of 5%, 14% and 14% (after test), respectively.
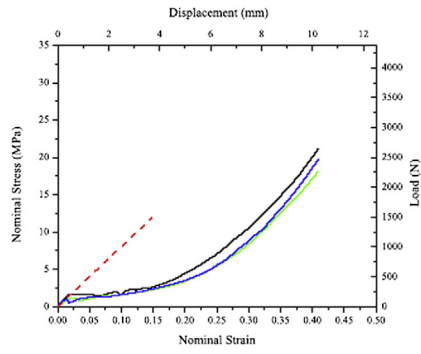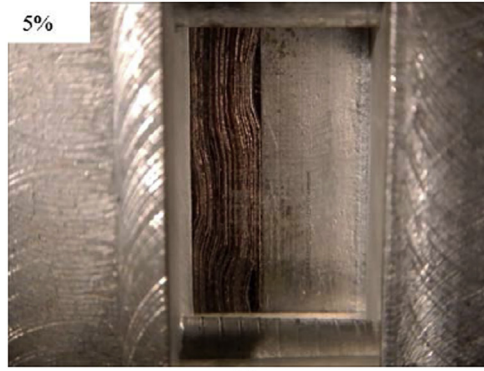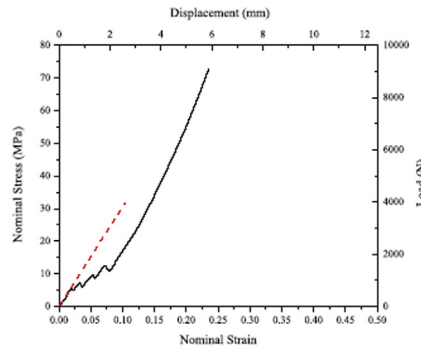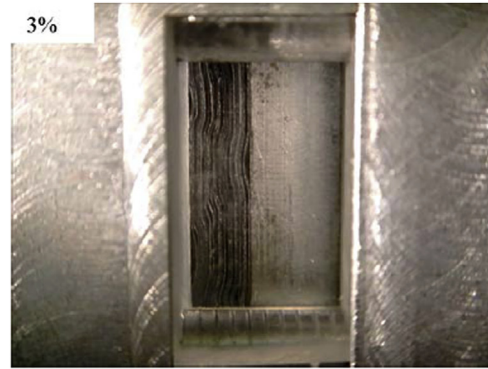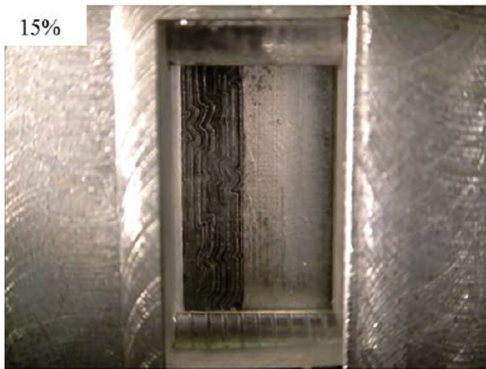
Fig. A2. (a) The in-plane nominal compressive stress–strain curves of anode specimens tested at a displacement rate of 0.5 mm min^{-1} (nominal strain rate of 0.0003 s^{-1}). (b–d) show the deformation patterns of an anode specimen at the nominal strains of 5%, 25%, and 40% (after test), respectively.

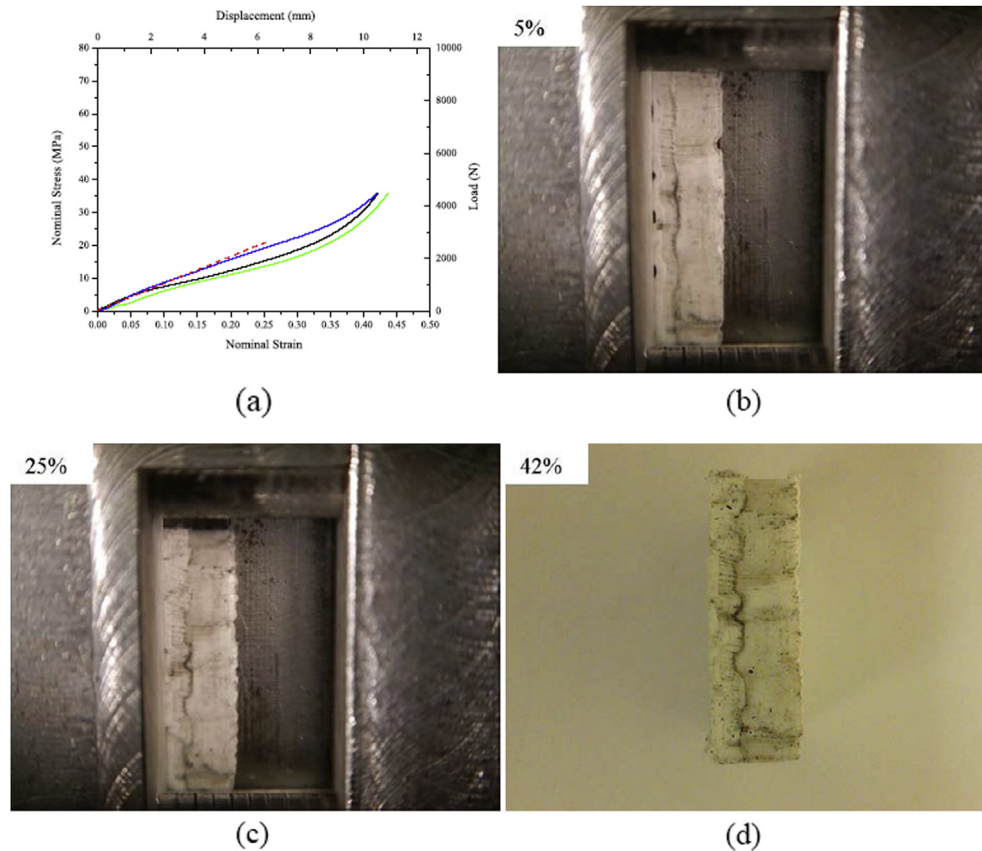**Fig. A3.** (a) The in-plane nominal compressive stress–strain curve of a cathode specimen tested at a displacement rate of 0.5 mm min^{-1} (nominal strain rate of 0.0003 s^{-1}). (b–d) show the deformation patterns of the cathode specimen at the nominal strains of 3%, 15%, and 24% (after test), respectively.

Fig. A4. (a) The in-plane nominal compressive stress–strain curves of separator specimens tested at a displacement rate of 0.5 mm min^{-1} (nominal strain rate of 0.0003 s^{-1}). (b–d) show the deformation patterns of a separator specimen at the nominal strains of 5%, 25% and 42% (after test), respectively.

References

[1] SAE J2464 NOV2009, Electric and Hybrid Electric Vehicle Rechargeable Energy Storage System (RESS) Safety and Abuse Testing, Society of Automotive Engineers, Warrendale, PA, 2009.

[2] J. Nguyen, C. Taylor, Safety Performance for Phosphate Based Large Format Lithium-ion Battery, in: Telecommunications Energy Conference, INTELEC 2004. 26th Annual International (2004), pp. 146–148.

[3] M. Otsuki, T. Ogino, K. Amine, ECS Transactions 1 (2006) 13–19.

[4] W. Cai, H. Wang, H. Maleki, J. Howard, E. Lara-Curzio, Journal of Power Sources 196 (2011) 7779–7783.

[5] E. Sahraei, R. Hill, T. Wierzbicki, Journal of Power Sources 201 (2012) 307–321.

[6] R. Hill, Development for a Representative Volume Element of Lithium-ion Batteries for Thermo-mechanical Integrity, Department of Mechanical Engineering, Massachusetts Institute of Technology, 2011.

[7] E. Sahraei, T. Wierzbicki, R. Hill, M. Luo, Crash Safety of Lithium-ion Batteries Towards Development of a Computational Model. SAE Technical Paper 2010-01-1078, Society of Automotive Engineers, Warrendale, PA, 2010.

[8] W. Lai, M.Y. Ali, J. Pan, Mechanical Behavior of Representative Volume Elements of Lithium-ion Battery Modules under Various Loading Conditions, Journal of Power Sources (2013), submitted for publication.

[9] M.Y. Ali, W. Lai, J. Pan, Journal of Power Sources 242 (2013) 325–340.

[10] M.Y. Ali, W. Lai, J. Pan, Computational Models for Simulation of a Lithium-ion Battery Module Specimen under Punch Indentation. companion paper to be submitted for publication (2013).

[11] W.C. Young, R.G. Budaynas, Roark's Formulas for Stress and Strain, seventh ed., McGraw-Hill, 2001.

[12] S. Timoshenko, Theory of Elastic Stability, McGraw-Hill, 1936.